Rare Met. (2023) 42(4):1160–1174
https://doi.org/10.1007/s12598-022-02220-w

RARE METALS

ORIGINAL ARTICLE

Highly efficient cobalt-based amorphous catalyst for peroxymonosulfate activation toward wastewater remediation

Xue-Chun Zhou, Shuang-Qin Chen*, Ming-Jie Zhou, Mai Li, Si Lan*, Tao Feng*

Received: 19 July 2022 / Revised: 26 September 2022 / Accepted: 27 September 2022 / Published online: 20 January 2023

Abstract Metallic glasses (MGs) are rising novae in the catalytic field, due to their unique amorphous structure, large residual stress, and high density of low coordination sites. However, there is still an absence of suitable MGs' catalysts for advanced oxidation processes (AOPs) with peroxymonosulfate (PMS), the most efficient and promising wastewater remediation technology. Herein, the cobalt-based MG (Co-MG) with a nominal composition of $Co_{67}Fe_4Mo_{1.5}Si_{16.5}B_{11}$ (at%) was utilized as an activator of PMS for azo dye degradation. The results demonstrated that the Co-MG/PMS system had an order of magnitude higher efficiency on Orange II (OII) degradation than the Fe-MG/PMS system. For fundamental study and field application, the effect of adding inorganic anions (Cl^-, HCO_3^-, $H_2PO_4^-$, SO_4^{2-}, NO_3^-), environmental factors, and cycle experiments on the catalytic properties of Co-MG were investigated emphatically to evaluate overall degradation performance. It has demonstrated that the Co-MG with more stability, better corrosion resistance and durability contrasted to Fe-MGs. In addition, the excellent catalytic performance of Co-MG was analyzed based on the quenched experiment, electron paramagnetic resonance (EPR), and X-ray photoelectron spectroscopy (XPS) analysis. The present results provide not only a new candidate but also shed light on exploring a new kind of AOPs system based on Co-MGs for wastewater treatment.

Keywords Co-based metallic glass ribbons; Inorganic ions; Stability; Advanced oxidation process; Peroxymonosulfate; Azo dyes

1 Introduction

Metallic glasses (MGs) in the catalytic field, as rising novae, have been attracting more and more attention due to their unique amorphous structure, thermodynamically metastable nature, and high density of low coordination sites [1–5]. Fe-based MGs, as the earliest amorphous alloy used for dye degradation, receive the most attention and indeed have catalytically active and uniquely selectivity in the remediation of wastewater [6–10]. For instance, Zhang et al. [11] developed $Fe_{78}Si_9B_{13}$ amorphous ribbons for the degradation of 3,5-dichlorosalicylic acid, which exhibited better catalytic performance in contrast to its crystallized counterpart and traditional crystalline Fe powder. Chen et al. [12] provided essential references for the Fe-based MG ($(Fe_{73.5}Si_{13.5}B_9Nb_3Cu_1)_{91.5}Ni_{8.5}$ nanocrystalline ribbons) used as a kind of Fenton-like catalyst in field applications and the development of advanced MGs with excellent adaptability to complex environments. Liang

Xue-Chun Zhou and Shuang-Qin Chen have contributed equally to this work.

Supplementary Information The online version contains supplementary material available at https://doi.org/10.1007/s12598-022-02220-w.

X.-C. Zhou, S.-Q. Chen*, M.-J. Zhou, M. Li, S. Lan*, T. Feng*
School of Materials Science and Engineering, Herbert Gleiter Institute of Nanoscience, Nanjing University of Science and Technology, Nanjing 210094, China
e-mail: chensq-hgi@njust.edu.cn

S. Lan
e-mail: lansi@njust.edu.cn

T. Feng
e-mail: tao.feng@njust.edu.cn

S.-Q. Chen*
School of Material Science and Engineering, Nanjing Institute of Technology, Nanjing 211167, China

et al. [13] reported a Fe-based MG with fine catalytic capacity for removing arsenic and nitrate (NO_3^-). However, for advanced oxidation processes (AOPs), the most efficient and promising wastewater remediation technologies, Fe-based MGs only show moderate catalytic performance [14]. It is urgent to develop novel MGs to better cooperate with AOPs for high-efficiency wastewater remediation.

AOPs are generally implemented by the addition of peroxymonosulfate (PMS), persulfate (PS) or hydrogen peroxides (H_2O_2) catalyzed to generate the strong oxidizing $SO_4^{\cdot-}$ and/or ·OH [15]. Among them, PMS is suitable for a wider pH range and the generated $SO_4^{\cdot-}$ possesses a higher oxidation potential and a longer half-life, which can better transfer mass and contact with the target compound [16]. Moreover, as a solid, PMS is easier to be stored and transported than liquid H_2O_2. In previous research, the catalytic activity of Co^{2+} for PMS is higher than that of Mn^{2+}, Ce^{3+}, Ni^{2+}, Fe^{2+}, V^{3+}, Ru^{3+}, etc. [17, 18]. In this light, cobalt-based MGs (Co-MGs) are expected to show excellent catalytic performance for AOPs. In previous reports, Co-MGs indeed were demonstrated to possess superior degradation performance in the redox remediation process of wastewater treatment. Qin et al. [19] reported the ultrafast degradation of azo dye by ball-milled Co-based MG powder. The apparent degradation rate constant (k_{obs}) of Co-based MG powder was an order of magnitude higher than that of the corresponding Co-based crystalline material with the same composition. Jiang et al. [14] investigated the azo dyes degradation performance of activated PDS under the synergistic catalysis of Fe and Co in amorphous alloys. Zeng et al. [20] also found that Co replaced partial Fe in the Fe-Si-B-P-Cu amorphous alloy ribbons promoted the degradation performance of methyl orange (MO) and enhanced physical adsorption and reduction ability of the ribbon to MO molecules. Recently, it was found that $Fe_{36}Co_{36}Si_{4.8}B_{19.2}Nb_4$ prepared by Co substituting for half of Fe in $Fe_{73.5}Si_{13.5}B_9Cu_1Nb_3$ could accelerate electron transport and obtain a higher degradation effect during AOPs [21]. Combined with the advanced catalytic performance of Co-based MGs and the catalytic activity of Co^{2+} for PMS, therefore, Co-based MGs are expected to present superior capability for recalcitrant wastewater remediation.

Herein, a Co-MG with nominal composition $Co_{67}Fe_4Mo_{1.5}Si_{16.5}B_{11}$ (at%, Co-MG) as PMS activator for the degradation of Orange II (OII) was reported originally in this work. The performance of Fe-MG was also investigated for comparison. The results demonstrated that Co-MG/PMS exhibited ten times higher degradation rate for OII than Fe-MG/PMS. The possible mechanism of high efficiency of Co-MG for sulfate-based AOPs was investigated systematically. This work provided not only a new candidate but also shed light on exploring a new kind of AOPs system based on Co-MGs for wastewater treatment.

2 Experimental

2.1 Chemicals

All reagents employed were of high purity grades without further purification. Peroxymonosulfate (PMS, $KHSO_5{\cdot}0.5KHSO_4{\cdot}0.5K_2SO_4$), furfuryl alcohol (FFA), benzoquinone (BQ), sodium hydroxide (NaOH), sodium chloride (NaCl), sodium bicarbonate ($NaHCO_3$), sodium sulfate (Na_2SO_4), sodium nitrate ($NaNO_3$) and sodium dihydrogen phosphate (NaH_2PO_4) were purchased from Aladdin Co., Ltd., China. 5,5-dimethyl-1-pyrroline N-oxide (DMPO) and tertiary butanol (TBA) were obtained from Adamas Reagent Co. Ltd. Other chemicals, including chromatographically pure methanol, ethanol, concentrated sulfuric acid (H_2SO_4, 98%) and hydrochloric acid (HCl, 37%) were provided by Guangzhou Fine Chemical Suppliers. Milli-Q ultrapure water with a resistivity of 18.2 MΩ·cm (25 °C) was used for all the experiments.

2.2 Preparation of catalysts

Alloy ingots were obtained by arc-melting of mixtures comprising Co, Fe, Mo, Si, B (purity 99.9%) elements under a high-purity Ar atmosphere. The amorphous alloy ribbons with the nominal composition of $Co_{67}Fe_4Mo_{1.5}Si_{16.5}B_{11}$ (at%, Co-MG) were manufactured from the above ingots via a single-roller melt-spinning process. The inside of the melting chamber was evacuated to a high vacuum condition of 1.2×10^{-3} Pa, and then filled with Ar atmosphere. The radio frequency melting was used to melt the mother alloy in the nozzle at induction current of 35–45 A. Then the molten metal was jetted from the nozzle orifice promptly onto the surface of the high-speed rotating copper rolls to continuously produce a rapidly solidified ribbon. The copper roll was rotated at a speed of 3500–4500 $r{\cdot}min^{-1}$. The FeSiB (Fe-MG) was prepared by a similar synthesis process as reported [22]. All the ribbon samples were preserved in an oxygen-free environment.

2.3 Characterizations

Scanning electron microscopy (SEM) images were recorded on JSM- IT500HR, and the surface morphologies of the ribbons after degradation experiments were characterized by an optical microscope (OM, ZEISSAxio). The

mappings of catalysts were carried out by X-ray energy-dispersive spectroscopy (EDS) in SEM to investigate the distribution of elements. The crystal structures of MG ribbons were analyzed by X-ray diffractometer (XRD, Bruker D8 Advance) in the 2θ range Cu Kα (λ = 0.154178 nm) radiation (40 kV, 40 mA). XPS data were acquired using a ULVCA-PHI spectrometer.

2.4 Degradation tests

The MG ribbons were cut into pieces with 10 mm × 10 mm as catalysts to conduct the degradation experiments. OII, as a typical azo dyes, was chosen to evaluate the catalytic performance of the prepared ribbons. Unless stipulated otherwise, all degradation tests were carried out via mixing 0.5 g·L^{-1} catalysts, 1.0 mol·L^{-1} PMS and 50 mg·L^{-1} OII in a 500 ml beaker which was placed in a water bath at 25 °C. Meanwhile, the reaction solution was maintained by stirring at 240 r·min^{-1} and then extracted via a peristaltic pump at specified time intervals for in situ analysis by ultraviolet-visible (UV-Vis) spectrophotometer. The pH of the solution was adjusted to a predetermined value using 1.0 mol·L^{-1} NaOH or 1.0 mol·L^{-1} HCl.

2.5 Analytical measurements

EPR (Bruker EMXplus, Germany) analysis and scavenging experiments were performed to identify the active species, and the free radicals and singlet oxygen ($^1O_2$) that formed in the PMS activation system were detected by using dimethyl pyridine N-oxide (DMPO) and 2,2,6,6-tetramethylpiperidine (TEMP) as spin trapping agents, respectively. The concentration of leached cobalt ions was detected by an inductively coupled plasma optical emission spectrometry (ICP-MS, ThermoFisher i CAPQ). The electrochemical tests were performed at (25 ± 1) °C via the traditional three-electrode cell by an electrochemical workstation (CHI660E, Shanghai Chen Hua Ltd., China). The ribbons with a side length of 10 mm were used as the working electrode, as well as the Pt sheet and SCE electrode were used as the counter electrode and the reference electrode, respectively. The electrolyte was OII (50 mg·L^{-1}) and NaCl (3.5%) solution as required. Based on the reported studies, the kinetic of OII degradation was evaluated by pseudo-first-order kinetics given in Eq. (1).

$$\ln\frac{C_t}{C_0} = -k_{\text{obs}} \tag{1}$$

where C_t is the OII concentration at actual time (t), C_0 is the initial OII concentration and k_{obs} is the rate constant.

3 Results and discussion

3.1 Catalyst characterization and performance

XRD patterns of as-prepared MG ribbons are presented in Fig. 1a. The samples both exhibited only a broad diffuse diffraction peak at the range of 40°–60°, and the amorphous state can be confirmed. The SEM images of Co-MG (Fig. 1b) and Fe-MG (Fig. S1) ribbons showed a uniform and dense surface, as well as the EDS mappings of Co-MG resulted that Fe, Co, Mo, and Si are uniformly distributed. Since the surface of the MG ribbons was so smooth that the adsorption tendency of organic pollutants could be ignored. Hence, it is not necessary to preset the adsorption–desorption equilibrium time before the degradation experiment. As shown in Fig. 1c, the catalytic performance of Co-MG was significantly better than that of Fe-MG under the same reaction conditions. Obviously, the OII removal rate of the Co-MG/PMS system reached 98.17% within 10 min and that of the Fe-MG/PMS system was only 17.22% at 60 min. The apparent degradation rate k_{obs} of the Co-MG/PMS system was 0.336 min^{-1}, while that of the Fe-MG/PMS system was inferior (0.025 min^{-1}). Co-MG/PMS system had an order of magnitude higher OII degradation rate than the Fe-MG/PMS system. Moreover, the apparent changes of catalytic discoloration and degradation of the OII dyes using the Co-MG/PMS system were shown in the UV spectrogram (inset in Fig. 1c). It can be found that the absorbance of the OII solution decreased rapidly during the reaction, and the intensity of the absorption peak at 484 nm corresponding to the –N=N– bond of OII almost disappeared at 10 min, which was due to the degradation of the chromophore. Further, the comparison between Fig. 1d, e indicated that the surface morphology of Co-MG did not change significantly after using it once, and only sporadic corrosion products existed. While the surface of the Fe-MG ribbons was almost entirely covered by granular intermediate products and partially exfoliated [23], the granular products aggregated at the exfoliated place. The still smooth and dense surface made the Co-MG ribbons reusable, which highlighted the superiority of Co-MG ribbons.

3.2 Evaluation of catalytic performances

3.2.1 Influence of reaction temperature

To further compare the catalytic abilities of Co-MG and Fe-MG, the activation energy of the degradation system was investigated. Figure 1f, g shows the effect of reaction temperature on the catalytic activity of Co-MG/PMS and Fe-MG/PMS system at different temperatures (25, 35, 45,

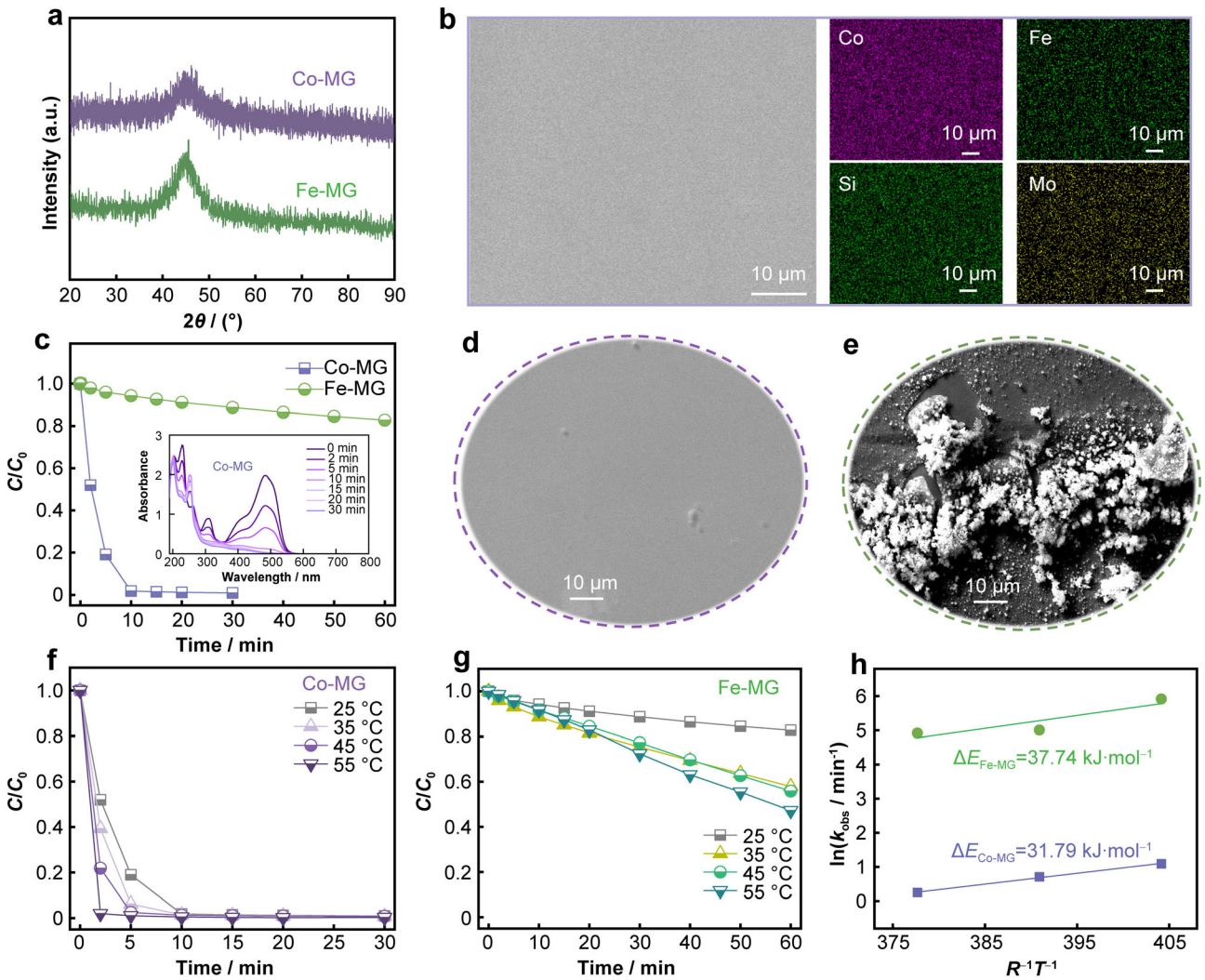

Fig. 1 **a** XRD patterns; **b** SEM image and EDS mappings of Co-MG; **c** comparison between Co-MG and Fe-MG on catalytic performance, and (inset) UV–Vis absorption spectra of degradation products of OII by Co-MG; SEM images results of the 1st run recycled **d** Co-MG and **e** Fe-MG ribbons; temperature effects of **f** Co-MG and **g** Fe-MG on OII removal; **h** Arrhenius equation analysis. (Catalyst: 0.5 g·L^{-1}, PMS: 1 mmol·L^{-1}, OII: 50 mg·L^{-1}, T = 25 °C)

55 °C), respectively. In the Co-MG/PMS system, the OII was almost completely decolored in 2 min at 55 °C. The pseudo-first-order reaction rate of the Co-MG/PMS system significantly boosted from 0.336 to 2.101 min^{-1}, while the degradation rate of the Fe-MG/PMS system slightly increased from 0.003 to 0.009 min^{-1}. As the temperature raised, the improvement of external thermal energy contributed to overcoming the reaction barrier for the chemical reaction, accelerating the catalytic reaction kinetics, and promoting the thermal activation of PMS, so that the degradation rate increased continuously. According to the Arrhenius equation: $\ln k_{obs} = \ln A - E_a/RT$, the activation energy (ΔE) of Co-MG (Fig. 1h) was calculated as 31.79 kJ·mol^{-1} and lower than that of Fe-MG ribbons (37.74 kJ·mol^{-1}), suggesting a better overall catalytic performance in AOP with PMS. Furthermore, with regard to most degradation reactions, the apparent activation energy is typically 60–250 kJ·mol^{-1}. The lower ΔE of MG ribbons indicated that the reaction energy barrier could be more efficiently [24].

3.2.2 *Influence of pH*

Besides the reaction temperature, other catalytic parameters, such as pH, OII amount, PMS concentration, and catalyst dosage, also significantly affect the OII removal rate. A detailed study on the relevant parameters was carried out to discuss the most suitable operating environment of the Co-MG/PMS system. From Fig. 2a, the outstanding catalytic degradation efficiency of the Co-MG/PMS system at pH = 5 or 9 is noticed, about 100% removal rate of OII was seen in 10 min, while the OII removal rate was lower

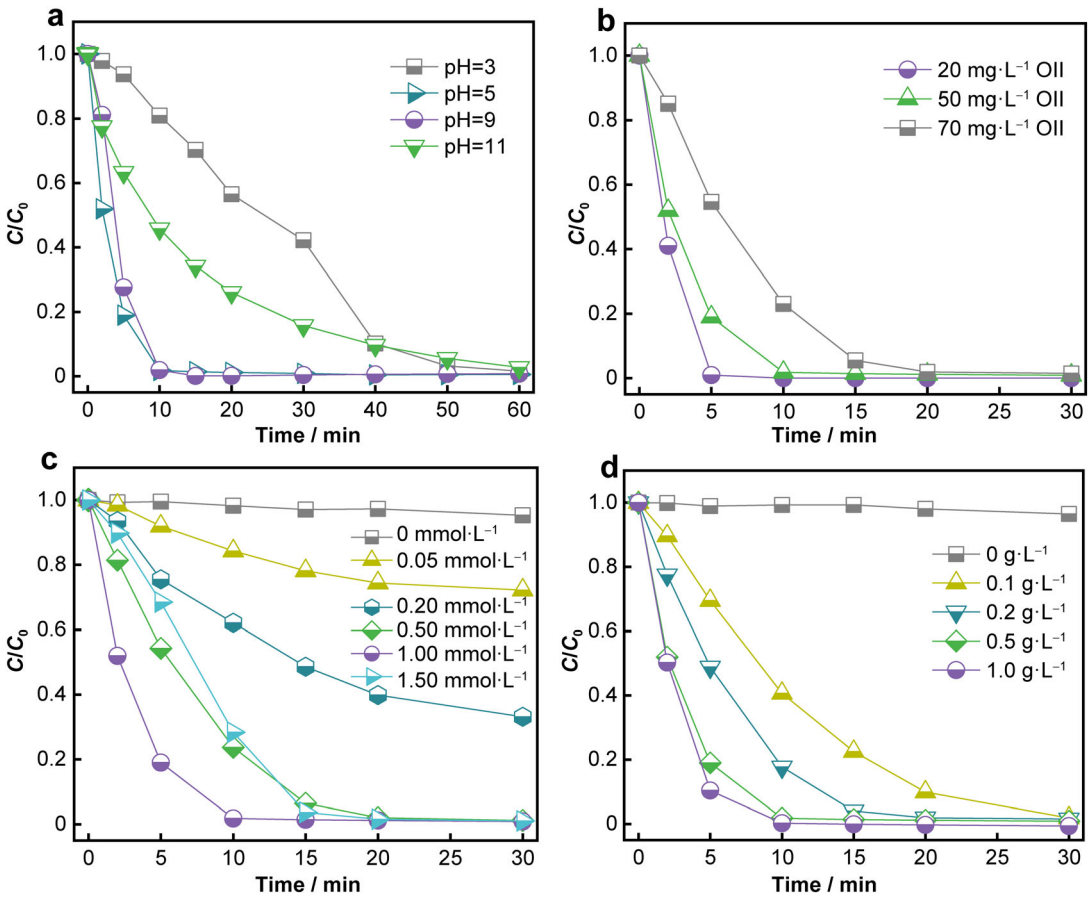

Fig. 2 Catalytic performance of different oxidation processes toward OII degradation: **a** effect on pH; **b** effect on OII amount; **c** effect on PMS concentration; **d** effect on catalyst dosage (catalyst: 0.5 g·L^{-1}, PMS: 1 mmol·L^{-1}, OII: 50 mg·L^{-1}, pH = 5, T = 25 °C)

at pH = 3 or 11. Obviously, the degradation effect of the Co-MG/PMS system was significantly inhibited under the condition of strongly acidic and base conditions. Reasons may be the following points. (i) When the reaction solution was acidic (pH = 3), the similar pH value to the PMS solution led to the problematic activation of the PMS. Moreover, the generated $SO_4^{\cdot-}$ and ·OH might be scavenged by H^+ (Reactions (2), (3)) [25, 26], and the quenching effect is noticeable. (ii) In contrast, the strong alkaline environment is not conducive to the Fenton-like reaction, and the Fe and Co elements on the surface of the MG ribbons react with OH^- to partially passivate at pH = 11, inhibiting the catalytic degradation reaction. In addition, when the pK_{a2} of PMS is 9.4, at pH = 11, most HSO_5^- decompose into SO_5^{2-}, and $SO_4^{\cdot-}$ would also react with OH^- to generate ·OH with lower oxidation (Reaction (4)), ·OH also might be scavenged by SO_5^{2-}, leading to inefficient degradation [27]. With regard to the positive factor in which PMS activation was favorable at pH = 5 and 9, the addition of a small amount of alkali accelerated the hydrolysis and ionization of PMS, namely, the amount of surface OH^- could activate PMS to generate $O_2^{\cdot-}$/$HO_2^{\cdot}$ radicals and a part of OH^- could be oxidized to ·OH by $SO_4^{\cdot-}$ (Reaction (4)), which contributed to the degradation of dyes. In any case, the Co-MG/PMS exhibited the outstanding ability of OII degradation within 60 min in a wide pH range.

$$SO_4^{\cdot-} + H^+ + e^- \rightarrow HSO_4^{\cdot-} \quad (2)$$

$$\cdot OH + H^+ + e^- \rightarrow H_2O \quad (3)$$

$$SO_4^{\cdot-} + OH^- \rightarrow \cdot OH + SO_4^{2-} \quad (4)$$

3.2.3 Influence of OII amount

As shown in Fig. 2b, when the OII amount increased from 20 to 50 and 70 mg·L^{-1}, the degradation efficiency depressed and the OII removal rate decreased from 0.483 to 0.336 and 0.129 min^{-1}, respectively. The more OII might largely induce this phenomenon adsorbed on the surface of the Co-MG ribbon, the more active sites were covered,

which inhibited the catalytic ability and deteriorated the degradation effect.

3.2.4 Influence of PMS concentration

Figure 2c shows the effect of oxidant PMS concentration on the OII degradation in the Co-MG/PMS system. Almost no reaction occurred when PMS was not present, indicating that Co-MG ribbon alone had poor reducibility to azo dyes and no degradation ability. This phenomenon was different from that of Fe-MG previously reported, which might be due to its higher corrosion resistance than iron. In addition, the OII degradation efficiency improved (k_{obs} increased from 0.071 to 0.336 min^{-1}) with the increase of PMS concentration (from 0 to 1 $mmol{\cdot}L^{-1}$). The higher concentration of PMS, the more active species generated through the activation of PMS by the Co-MG ribbon, resulting in a higher degradation rate. However, once the PMS concentration was excessive (1.5 $mmol{\cdot}L^{-1}$), the removal rate of OII was instead inhibited. The possible reasons were as follows: on the one hand, there were not enough active sites on the surface of the amorphous ribbons to activate excessive PMS; on the other hand, radicals generated by PMS activation and excess PMS reacted with each other. As shown in Reactions (5–7), HSO_5^- reacted with $SO_4^{\cdot-}$ or ·OH to produce $SO_5^{\cdot-}$ with weaker oxidizing, which also adversely depressed the degradation rate.

$$HSO_5^- + SO_4^{\cdot-} \rightarrow HSO_4^- + SO_5^{\cdot-} \quad (5)$$

$$HSO_5^- + \cdot OH \rightarrow SO_5^{\cdot-} + H_2O \quad (6)$$

$$SO_5^{2-} + SO_4^{\cdot-} \rightarrow SO_5^{\cdot-} + SO_4^{2-} \quad (7)$$

3.2.5 Influence of catalyst dosage on OII degradation

Distinctly, it can be seen from Fig. 2d that the catalyst dosage positively affected the degradation efficiency of OII. The system without Co-MG (catalyst), only PMS existed, had no degradation performance. With the increase of catalyst dosage from 0.1 to 1.0 $g{\cdot}L^{-1}$, the catalysis functions were significantly improved, and the first-order degradation rate constant was raised from 0.077 to 0.376 min^{-1}. The additive amount of Co-MG contributed to a large proportion of the overall OII removal rate due to the more catalyst with the more active sites and the more fully contacted Co-MG/PMS/OII system, which improved catalytic degradation efficiency.

3.2.6 Influence of inorganic anions

Various inorganic anions widely exist in industrial wastewater and actual water bodies, which impact the degradation efficiency in very complicated ways, consisting of scavenging radicals ($SO_4^{\cdot-}$ or ·OH), adjusting the pH values, or competing with organic pollutants. Hence, the effect of Cl^-, HCO_3^-, $H_2PO_4^-$, SO_4^{2-}, NO_3^- on OII degradation was carried out, as shown in Fig. 3a–e. By the way, considering eliminating the interference of metal cations, sodium salts were uniformly used for the experiments. The pseudo-first-order kinetic model fitted the curve of the normalized concentration change, and the apparent shift of OII k_{obs} with respect to the concentration and species of inorganic anions is obtained from Fig. 3f. All the inorganic anions exhibited more or less inhibitory effects on the oxidation processes. Interestingly, when a small amount of Cl^- (1 $g{\cdot}L^{-1}$) was added to the OII solution, the degradation performance of the Co-MG/PMS system was pelter (Fig. 3a). Nevertheless, adding Cl^- (from 1 to 30 $g{\cdot}L^{-1}$), the degradation rate of OII sostenuto increased. When the concentration of Cl^- reached 30 $g{\cdot}L^{-1}$, the k_{obs} value was up to 0.260 min^{-1}, and the catalytic degradation performance was comparable to that without Cl^-. The addition of Cl^- can convert $SO_4^{\cdot-}$ and ·OH into $Cl^{\cdot}$, $Cl_2^{\cdot-}$ and $ClOH^{\cdot-}$ (Reactions (9–11)), which weakens the catalytic properties. In contrast, when Cl^- was over a critical concentration, it caused that Cl^- and PMS (HSO_5^-) reacted directly through a two-electron transfer reaction to generate Cl_2 and HClO (Reactions (12, 13)) which participated in the degradation of OII [28, 29]. In other words, the generated Cl_2 and HClO in a significant amount would rapidly bleach dyes so the degradation efficiency was continuously improved. This process of first inhibition and then promotion with the increase of Cl^- concentration is consistent with the double effect of Cl^- as previously reported [30].

$$SO_4^{\cdot-} + Cl^- \rightarrow Cl^{\cdot} + SO_4^{2-} \quad (8)$$

$$Cl^{\cdot} + Cl^- \leftrightarrow Cl_2^{\cdot-} \quad (9)$$

$$\cdot OH + Cl^- \rightarrow ClOH^{\cdot-} \quad (10)$$

$$2Cl_2^{\cdot-} \rightarrow Cl_2 + 2Cl^- \quad (11)$$

$$2Cl^- + HSO_5^- + H^+ \rightarrow SO_4^{2-} + Cl_2 + H_2O \quad (12)$$

$$Cl^- + HSO_5^- \rightarrow SO_4^{2-} + HOCl \quad (13)$$

In a similar condition, HCO_3^- also had a dual effect on the catalytic performance (Fig. 3b) [31], but the overall inhibition effect of OII degradation was more prominent. HCO_3^- concentration at 1 $g{\cdot}L^{-1}$ had the most significant inhibitory effect, showing the highest inhibitory effect on OII degradation among all inorganic anions, and the k_{obs} value was only 0.026 min^{-1}. HCO_3^- can also quench $SO_4^{\cdot-}$/·OH (Reactions (14, 15)) to generate $CO_3^{\cdot-}$ with a lower redox potential of 1.59 V. In addition, HCO_3^- also consumed OH^- in solution, impeding the activation of PMS by bases, which was detrimental for the degradation. The inhibition of degradation slightly weakened with

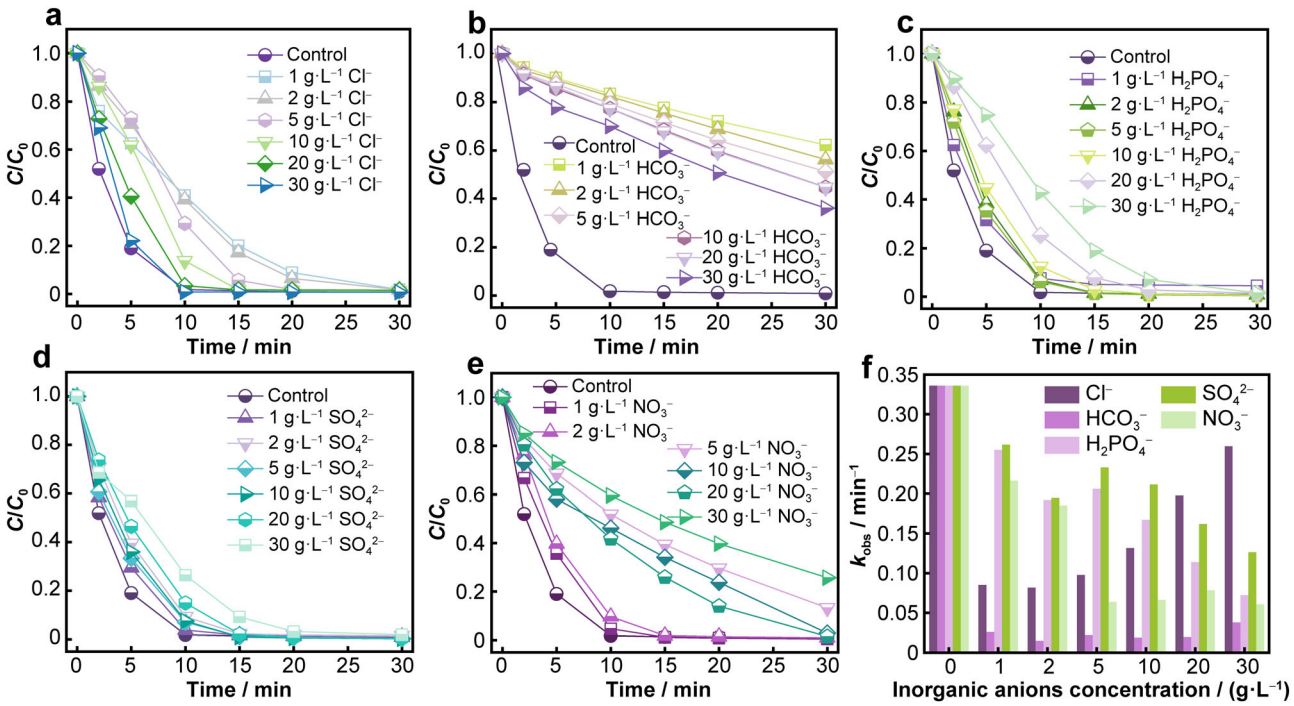

Fig. 3 Effects of **a** Cl^-, **b** HCO_3^-, **c** $H_2PO_4^-$, **d** SO_4^{2-}, **e** NO_3^- on OII degradation in Co-MG/PMS system, and **f** change of OII k_{obs} with different concentrations of inorganic anions (catalyst: 0.5 g·L^{-1}, PMS: 1 mmol·L^{-1}, OII: 50 m g·L^{-1}, pH = 5, T = 25 °C)

increasing HCO_3^- concentration. Considering HCO_3^- as a buffer reagent, it has a regulatory effect on pH value to stimulate PMS decomposition and supply a weakly alkaline environment (pH value in the range of 5 to 8) [32]. According to the research on the effect of pH on OII degradation (Fig. 2a), in the case of weak acid to weak base conditions, there was almost no effect on the degradation rate of OII. Therefore, the effect of HCO_3^- on pH can be excluded. Furthermore, the more HCO_3^-, the less OH^- was depleted, and the extra OH^- increased for activation of PMS. In fact, Yang et al. [33] reported that HCO_3^- can activate PMS, and the produced active species may somewhat relieve the inhibitory effect.

$$SO_4^{\cdot-} + HCO_3^- \rightarrow CO_3^{\cdot-} + SO_4^{2-} + H^+ \quad (14)$$

$$\cdot OH + HCO_3^- \rightarrow CO_3^{\cdot-} + H_2O \quad (15)$$

Figure 3c–e depicts that OII degradation was dropped down in the presence of $H_2PO_4^-$, SO_4^{2-}, NO_3^- (from 0 to 30 g·L^{-1}). The corresponding k_{obs} values of Co-MG/PMS/anions system also reduced, as clearly observed from Fig. 3f. Analogously, $H_2PO_4^-$ and NO_3^- can both scavenge $SO_4^{\cdot-}$/·OH and generate weaker secondary radicals of $H_2PO_4^{\cdot}$ and $NO_3^{\cdot}$ (Reactions (16–19)), and the effect is monotonic [34]. Actually, phosphate and sulfate, as the typical complex ions, could decrease the active cobalt species on the Co-MG surface group through chelating reactions in a natural water. With regard to the addition of SO_4^{2-}, the solution inevitably contained SO_4^{2-} due to PMS as a complex persulfate. A similar trend has also been reported by Long et al. [35], which found that SO_4^{2-} had an inhibitory action on the degradation rate. This phenomenon was mainly attributed to the lower redox potential of $SO_4^{2-}/SO_4^{\cdot-}$, which reduced the amount of $SO_4^{\cdot-}$ in the solution. There were differences in the degree of unidirectional inhibition exhibited by the three inorganic anions. Although $H_2PO_4^-$ and $SO_4^{\cdot-}$ cut down the reaction rate, the Co-MG/PMS system still degraded OII entirely within 30 min, indicating that there were enough active substances for OII degradation in the solution.

$$H_2PO_4^- + SO_4^{\cdot-} \rightarrow H_2PO_4\cdot + SO_4^{2-} \quad (16)$$

$$H_2PO_4^- + \cdot OH \rightarrow H_2PO_4\cdot + OH^- \quad (17)$$

$$NO_3^- + SO_4^{\cdot-} \rightarrow NO_3\cdot + SO_4^{2-} \quad (18)$$

$$NO_3^- + \cdot OH \rightarrow NO_3\cdot + OH^- \quad (19)$$

In order to further explore the effect of inorganic anions on the Co-MG/PMS system. A series of characterizations were performed on the used Co-MG ribbons in the systems containing different inorganic anions. As observed in Fig. 4a, XRD patterns for Co-MG used in other anions still showed a broad diffraction peak without any crystalline diffraction, confirming the remains of the amorphous structure. The surface morphologies of the Co-MG ribbons after degradation in the presence of various anions were examined carefully by OM and SEM, due to the surface-mediated process on the degradation of azo

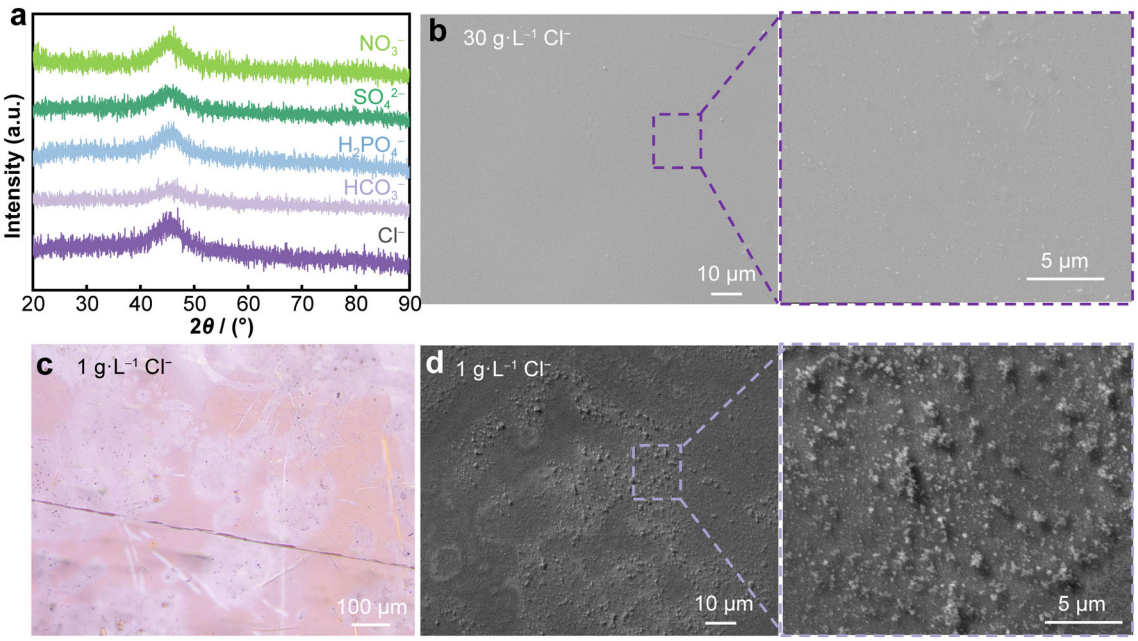

Fig. 4 **a** XRD patterns; **b** SEM images of Co-MG after OII degradation in presence of 30 g·L^{-1} Cl^{-}; **c** surface morphology and **d** SEM images of Co-MG after OII degradation in presence of 1 g·L^{-1} Cl^{-}

dyes. It can be seen that there was a bit of micron-sized particles appeared on the surface of Co-MG after OII degradation in the presence of $H_2PO_4^-$, SO_4^{2-}, NO_3^-, and the rest of the amorphous ribbons was almost in good condition (Fig. S2a–c). This phenomenon also corresponded to the brighter OM images without plentiful cracks (Fig. S3a–c). Distinctly, in the presence of HCO_3^-, the SEM images of Co-MG displayed a bit of micron-sized particles and even some flocs on the surface of Co-MG ribbons. The aforementioned floccule may be intermediate products during the degradation reaction (Fig. S3d). Furthermore, the more intermediate products, which corresponded to the dark region of Fig. S4d, covered the active surface of the Co-MG ribbons, leading to the inhibition of the catalytic degradation properties. This result also coincided with the worst degradation effect with HCO_3^- as shown in Fig. 3.

Interestingly, when the addition amount of Cl^- increased to 30 g·L^{-1}, micron-sized particles were sparsely scattered on the surface of the Co-MG ribbons. In contrast, the large amounts of sediments which might be the visible degradation products can be observed on that in the presence of 1 g·L^{-1} Cl^- from Fig. 4d, and the center of the main reacted region was relatively flat with some cracks as shown in Fig. 4c. This phenomenon also perfectly explained the inhibitory effect of Cl^- on OII degradation at low concentrations (1 g·L^{-1}). What's more, the generated Cl_2 and HClO in a great amount exhibited strong oxidability (30 g·L^{-1} Cl^-), most of the granular intermediates that covered surface of Co-MG ribbons were degraded and peeled off. The re-exposed active surface was beneficial in improving the catalytic efficiency. Besides these, the leaching value of Co^{2+} in the Co-MG/PMS/OII system in the presence of various inorganic anions is revealed in Fig. S5. It can be clearly seen that a small quantity of Co^{2+} leaches in the presence of HCO_3^- and NO_3^-. This phenomenon corresponded to the OII degradation rate according to the fewer of Co^{2+} as an active substance in the reaction solution. As an efficient catalyst to degrade OII, the Co-MG ribbons were suitable for the most inorganic anions and the broad pH range. The broad prospects of the Co-MG/PMS system for application in actual water bodies were expected.

3.3 Stability, recyclability, and corrosion properties of Co-MG catalyst

In general, reusability is an important indicator for estimating catalyst performance, thus, it is the stability of heterogeneous catalysts in the Co-MG/PMS system that is of great significance in practical application. Moreover, before each catalytic recyclability test, the surface of the Co-MG ribbon was washed three times with deionized water, and the next round of degradation was performed immediately. Since the surface morphology and composition of Co-MG did not change significantly after the first cycle (Fig. 1d), and the ribbons used for multiple processes still maintained the amorphous structure (Fig. S6), the highly efficient catalytic ability of Co-MG ribbons was expected during the recycling experiment. The results are

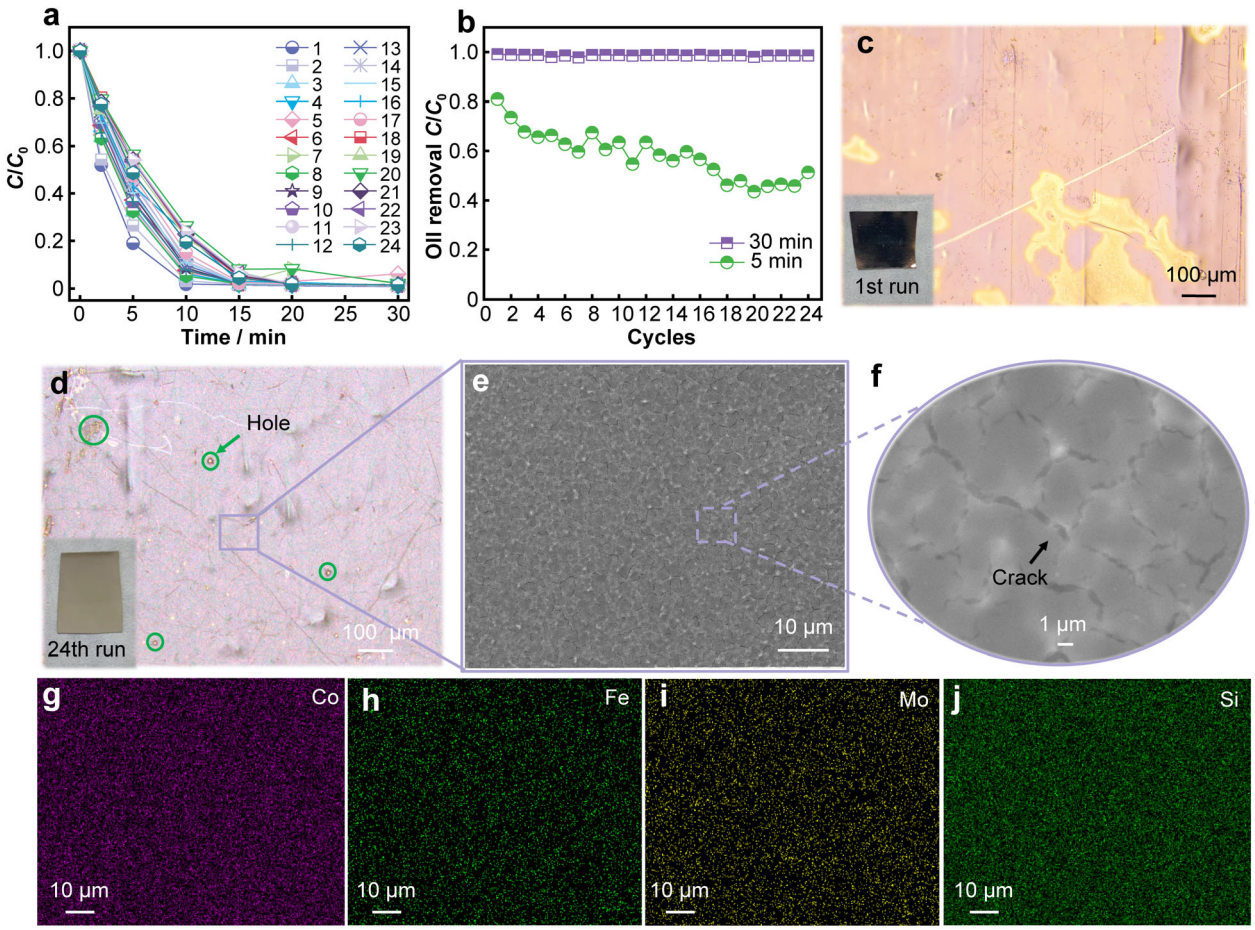

Fig. 5 **a** Reusability tests of Co-MG for OII degradation with 1–24 cycles; **b** OII removal rate at 5 and 30 min-degradation over 24 cycles; OM images of Co-MG ribbons used after **c** 1 cycle and **d** 24 cycles; **e** SEM images of Co-MG ribbons used after 24 cycles and **f** magnification diagram; corresponding EDS mappings of **g** Co, **h** Fe, **i** Mo, **j** Si (catalyst: 0.5 g·L^{-1}, PMS: 1 mmol·L^{-1}, OII: 50 mg·L^{-1}, pH = 5, T = 25 °C)

presented in Fig. 5. The OII removal rate was still stable above 97% after 30 min over the multiple cycles (within 24 cycles), even if the degradation efficiency of OII displayed a downward trend at 5 min for various runs, from 81.06% to 51.33% (Fig. 5b). It was proved that although the performance of Co-MG was slightly attenuated during repeated use, it still maintained extremely high degradation performance under experimental conditions thus Co-MG ribbons had excellent recyclability and stability. Meanwhile, the surface of the ribbons after using 24 times is observed in Fig. S5, covered by off-white substances entirely and uniformly, yet there was no apparent difference between the original ribbons and the ribbons for the first cycle. Accordingly, many holes and cracks due to corrosion were observed on the surface of Co-MG ribbons in Fig. 5d. If these cracks expand, the porous reaction zone and the precipitated oxidation products tend to fall off automatically, forming pores on the surface [36]. The enlarged SEM images of the ribbons for the 24 cycles have further illustrated the presence of numerous microcracks (Fig. 5e, f), and the cracks disclosed the unreacted parent ribbon matrix and exposed fresh active sites. In addition, a large number of uniformly distributed Fe, Co, Mo, Si elements can be detected, as shown in the EDS mappings of Fig. 5g–j. Compared with the original Co-MG ribbons, the relative content of the O element exhibited an enormous growth, and the poorer Co element was consumed as the main active species (Table S1), indicating that the elements on the surface of the Co-MG ribbons were oxidized to a large extent. Among them, the change of Si relative content can be ignored, which was attributed to that the amorphous silicon is easily oxidized to SiO_2, which was the main component of the spalling layer [7]. Although the SiO_2 and HBO_2/H_3BO_3 protective layer depressed the catalytic performance, to a greater extent, it impeded the leaching of cobalt ions and further protected the buried active Co species [11, 37]. Therefore, the Co-MG ribbons exhibited high stability over 24 cycles. Moreover, the oxides and

hydroxides of the surface low-valence metal elements can still be used as active sites for activating PMS, ensuring the efficient catalytic ability of the Co-MG/PMS system.

Generally, the degradation process was involved in the redox reaction, so the electron transfer played a crucial role on the surface of ribbons and was also related to the corrosion resistance [38]. As shown in Fig. 6a, b, the open circuit potential (OCP) and the polarization curves of the Fe-MG and Co-MG ribbons in OII and NaCl solutions. Both stabilized E_{OCP} (the open circuit potential) values of Co-MG ribbons in different solutions were apparently higher than that of Fe-MG ribbons. The more positive E_{OCP} value of Co-MG ribbons indicated higher corrosion resistance [39]. The fast corrosion of Fe-MG ribbon could consume a great deal of the catalyst so it debased its endurance, which was not desirable for its application. Besides, the Co-MG performed visibly lower corrosion current densities, confirming its better corrosion resistance in whether OII or NaCl solution.

According to Nyquist curves in Fig. 6c, Co-MG ribbons showed a longer radius of Nyquist semicircles in NaCl solution (the corrosive solution), implying their better corrosion resistance, which also agreed well with the polarization results. Interestingly, in the OII solution (the catalytic environment), the lower charge transfer resistance for the Co-MG ribbons illustrated a faster surface reaction rate with effective charge transfer than Fe-MG ribbons, which also indirectly proved that Co-MG has a stronger catalytic ability than Fe-MG. These results further confirmed the enhanced catalytic activity and cycling stability of cobalt-based amorphous ribbons.

3.4 Mechanistic investigation

In order to clarify the contribution of active species in the OII degradation process by the Co-MG ribbons, the quenching experiments and EPR test were carried out. As shown in Fig. 7a, the addition of 10 mmol·L^{-1} TBA had a slight effect on the OII degradation reaction, and a ten-fold concentration of that (100 mmol·L^{-1} TBA) still showed a similarly weak inhibitory effect, indicating that ·OH was not the main active species in the Co-MG/PMS/OII system. Correspondingly, adding the same concentration of quencher (10 to 100 mmol·L^{-1}), a dramatically inhibitory effect by MeOH on OII removal efficiency illustrated that the contribution of $SO_4^{\cdot-}$ should be more dominant. Figure 7b shows the effect of different quenchers on OII degradation in the Co-MG/PMS system intuitively. Interestingly, EPR spectra showed a weaker DMPO-$SO_4^{\cdot-}$ signal, while the characteristic peak intensities of DMPO-·OH (1:2:2:1) were observed (Fig. 7c) [40]. The phenomenon might be mainly due to the existence of OH^- which originated from NaOH used for pH regulation, and the generous $SO_4^{\cdot-}$ could react with OH^- to generate ·OH (Reaction (4)). In addition, using BQ as a particular $O_2^{\cdot-}$ quencher, as well as the quenching tests using FFA and L-histidine were performed to determine whether $^1O_2$ dominated the OII degradation [41]. A distinct inhibitory effect can be seen in Fig. 7a by adding BQ while the FFA and L-histidine can completely inhibit the OII degradation, indicating that the $O_2^{\cdot-}$, as an intermediate product to form $^1O_2$ (Reaction (20)), played a crucial role in mediating OII degradation. Moreover, $O_2^{\cdot-}$ could be generated in the presence of dissolved oxygen (Reaction (21)). Besides, TEMP as a spin trap agent emerged a characteristic triple peak (1:1:1) which was concrete evidence for the existence of $^1O_2$ (Fig. 7d) [42]. Actually, the self-decomposition of PMS also generates $^1O_2$ [43]. The $^1O_2$ signal in Co-MG/PMS/OII system was weaker, which indicated the production of $^1O_2$ as active species were consumed to degrade OII.

$$O_2^{\cdot-} + \cdot OH \rightarrow OH^- + {}^1O_2 \quad (20)$$

$$O_2 + e^- \rightarrow O_2^{\cdot-} \quad (21)$$

Furthermore, to reveal the relationship between the surface chemical valence state and catalytic performance of Co-MG ribbons, XPS analysis was performed on the ribbon's surfaces before and after the degradation reaction.

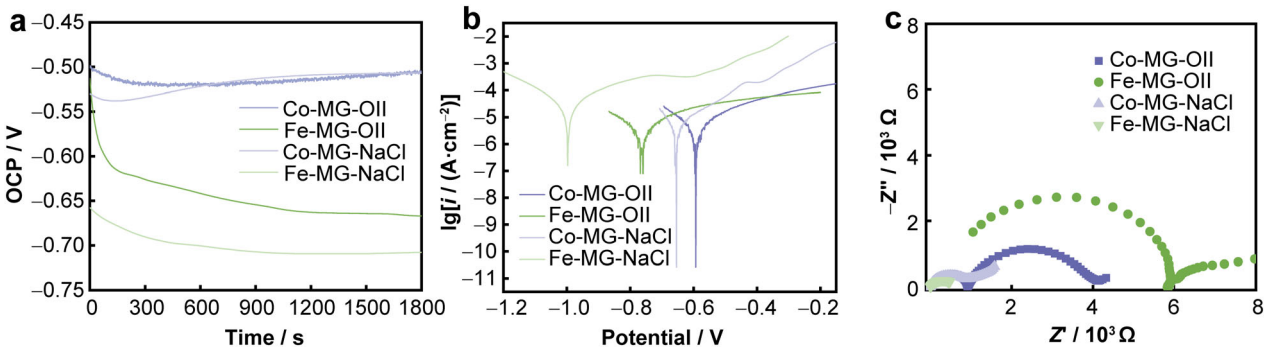

Fig. 6 **a** OCP, **b** potentiodynamic polarization and **c** Nyquist curves of Co-MG and Fe-MG ribbons in OII and NaCl solutions

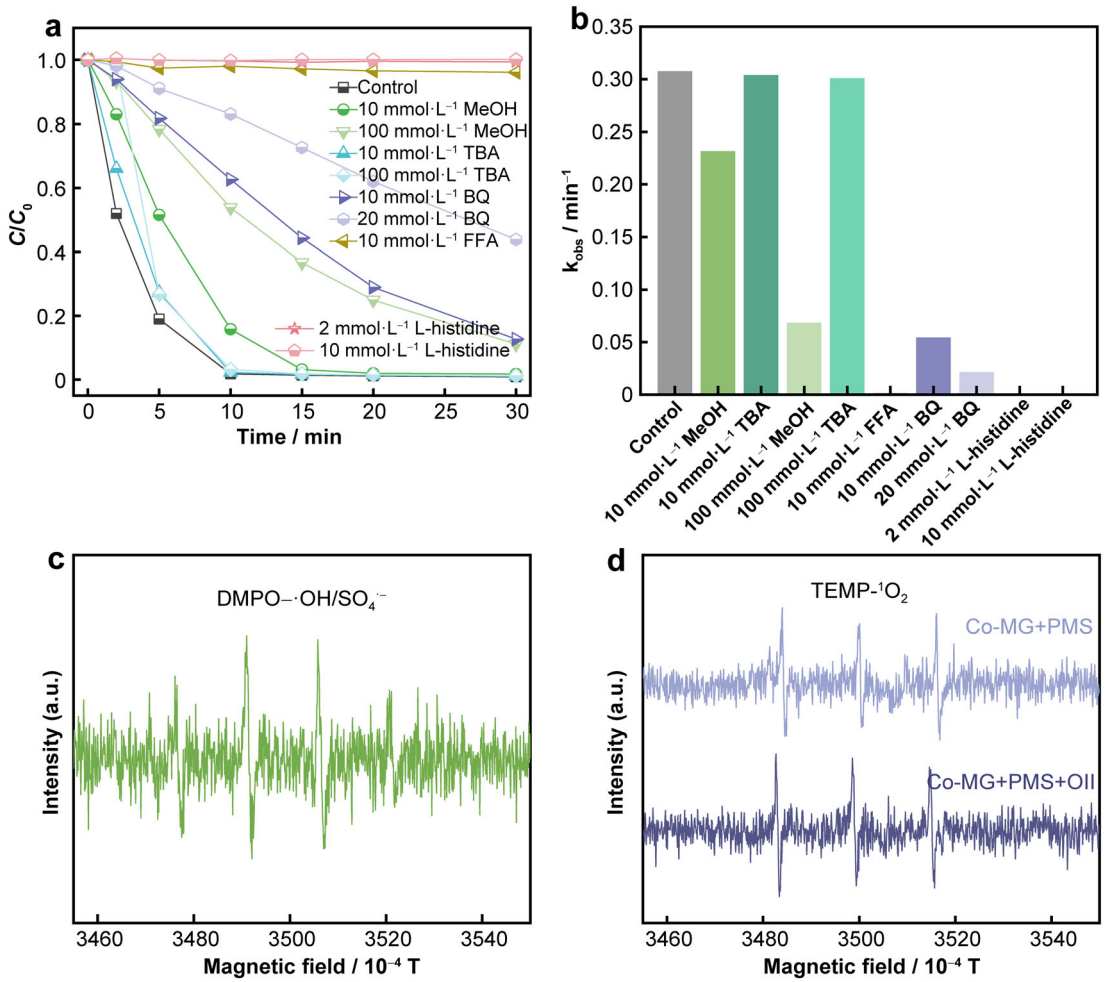

Fig. 7 **a** Effect of different quenchers on OII degradation in Co-MG/PMS system and **b** corresponding rate constant with 15 min; EPR spectra in Co-MG/PMS system with **c** DMPO and **d** TEMPO as trapping agent (catalyst: 0.5 g·L^{-1}, PMS: 1 mmol·L^{-1}, OII: 50 mg·L^{-1}, pH = 5, T = 25 °C)

As shown in Fig. 8a, compared with the original Co-MG ribbons, the Co 2p and Fe 2p peaks become obviously weak, while the intensity of the O 1s peaks was increased after degradation experiments. The results suggested that Co and Fe elements as active sites were depleted, and the oxidation reaction occurred on the surface of Co-MG ribbons. Nevertheless, the Co 2p spectrum of the Co-MG ribbons showed peaks at 778.2, 780.8, 782.3 and 786.6 eV, which belonged to Co^0, Co^{2+}, Co^{3+} and satellite peak, respectively (Fig. 8b) [44, 45]. After being reused, the peak representing Co^0 disappeared gradually. Interestingly, the concentration of Co^{2+} reduced after the first run while increased after the 24th run (from 43.5% to 40.06% to 47.66%) and Co^{3+} gradually appeared during the degradation in Table S2, which might be attributed to the depletion of Co^{2+} as the active species and then the surface oxide layer was cracked or even corroded to expose the original ribbons. A similar phenomenon can be found in Fig. 8c. Metallic Fe^0 was completely transformed to Fe^{2+} and Fe^{3+} in the reused glassy ribbons. The peaks at 707.0, 711.3 and 714.1 eV corresponded to Fe^0, Fe^{2+} and Fe^{3+}, respectively. Although Fe was not the main metal element of the amorphous ribbons, a small amount of low-valence Fe can transfer electrons to Co^{3+}, promote the reduction of Co^{3+} to Co^{2+}, maintain the high content of Co^{2+} in the ribbons, or directly transfer electrons to the PMS to promote degradation reaction. Concerning the results of the changes in the Co and Fe valence states also reflected the stability and high catalytic performance of the amorphous ribbons [46]. In addition to the peak analysis of O 1s (Fig. 8d), the peak at 529.9 eV was attributed to the lattice oxygen in Co-MG and the content of $O_{latt.}$ decreased from 33.21% to 17.21%, which suggested the consumption of metal–oxygen to participate in the reaction. What's more, the reactive $O_{latt.}$ generated could form oxygen vacancy on the catalyst surface, promoting the generation of the non-

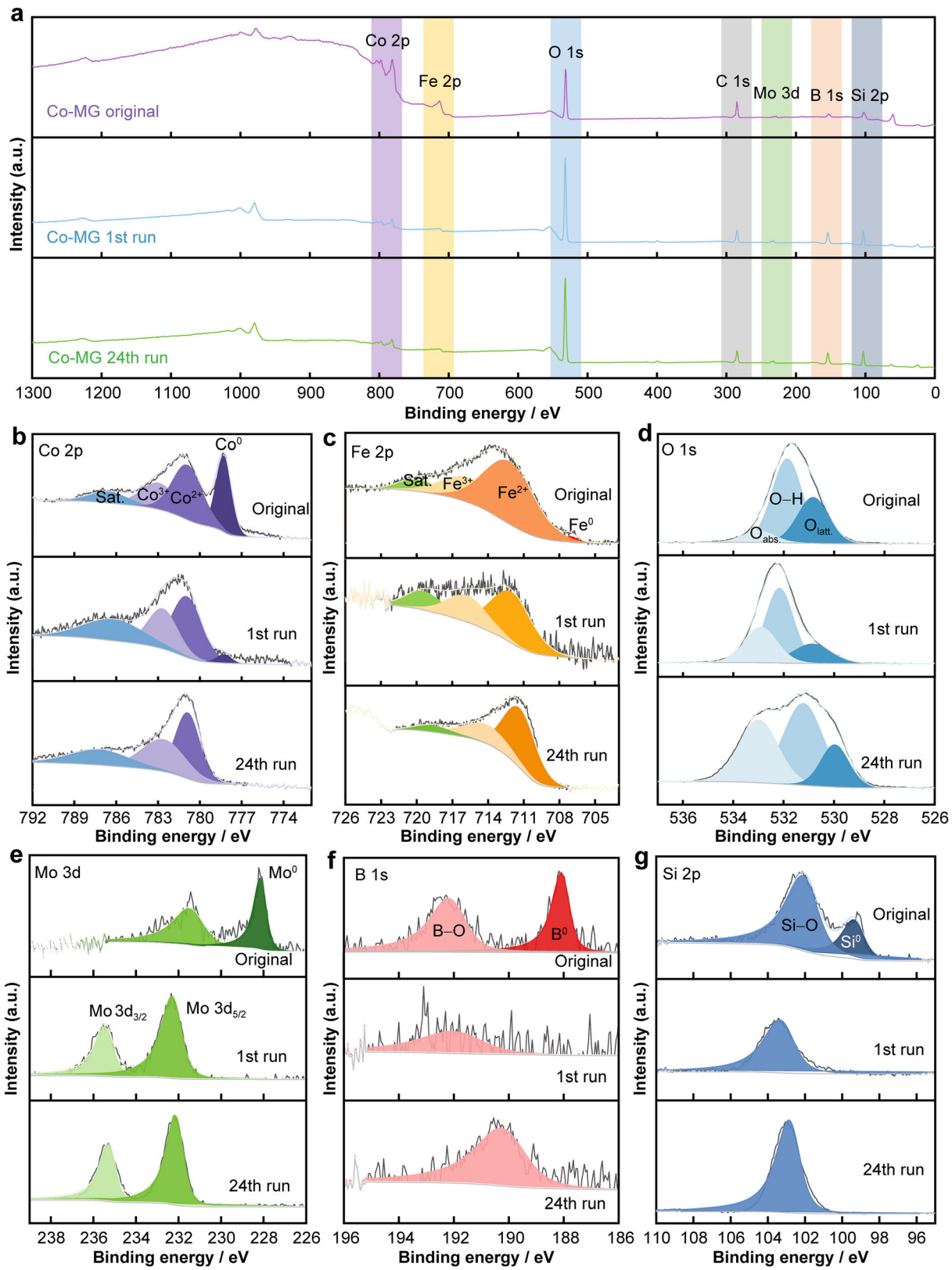

Fig. 8 **a** XPS wide-scan survey of Co-MG in different states, including original, used after the 1st run and 24th run; **b** Co 2p, **c** Fe 2p, **d** O 1s, **e** Mo 3d, **f** B 1s, **g** Si 2p spectra of fresh and used Co-MG

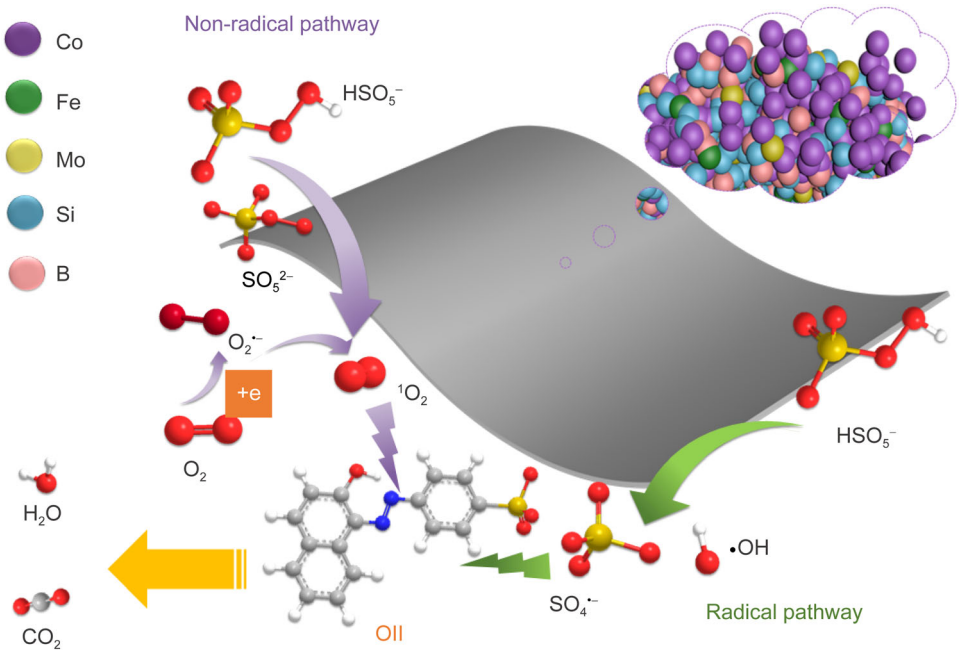

Fig. 9 Possible mechanism of PMS activation by Co-MG for OII degradation

radicals to boost catalytic reaction further. The other peaks at 531.8 and 532.9 eV correspond to the characteristic of hydroxide (OH^-) and Si–O–Si band/adsorbed H_2O, respectively. For Mo 3d (Fig. 8e), the binding energies located at 228.3, 232.2 and 235.5 eV are attributed to Mo^0, Mo $3d_{3/2}$ and Mo $3d_{5/2}$, respectively. The B^0 and B–O bonds with binding energies at 188.1 and 192.2 eV can be observed in Fig. 8f [47]. The peaks attributing Mo^0 and B^0 disappeared after degradation, implying that they were involved in the redox reaction. The peak for Si^0 at 99.1 eV disappeared after reuse, and the proportion of the Si–O peak (102.6 eV) increased (Fig. 8g), further affirming the formation of the oxide layer (SiO_2) during the catalytic performance [21, 48]. According to the above results, the reductive Co^0, Fe^0, Mo^0, B^0 and Si^0 were observed on the Co-MG surface and might act as electron donors in the degradation process. Lower valence band positions required less energetic activation, providing better electron transfer efficiency during the reductive OII degradation. According to the above analysis, a possible catalytic degradation mechanism was presented. The entire reaction process takes place on the surface of the catalyst. The PMS was catalyzed to generate $^1O_2$ and free radicals ($SO_4^{\cdot-}$ and ·OH) with strong oxidizing properties to degrade organic pollutants into small molecular products (Fig. 9). Moreover, the chromophore group easily becomes excited electrons, thereby activating the partial structure of the molecule, making the carbon atom connected to the azo group unstable, and then promoting the C–N bond crack.

4 Conclusion

In this work, a highly efficient AOP system, Co-MG/PMS, possessed an order of magnitude higher k_{obs} (0.336 min^{-1}) than the Fe-MG/PMS system (k_{obs} = 0.025 min^{-1}) for OII degradation has been developed. The superior catalytic performance of Co-MG for PMS during AOP can be attributed to the lower activation energy of Co-MG (31.79 $kJ{\cdot}mol^{-1}$), a synergistic effect of elements, and unique catalytic mechanism with dominant active species of $^1O_2$. In addition, the Co-MG ribbon showed excellent durability, as indicated that the organic pollutant OII was degraded entirely within 30 min after 24 cycles due to high corrosion resistance. Meanwhile, the influences of various important essentials on OII degradation were comprehensively studied, as well as the results demonstrated that Co-MG/PMS system exhibited excellent adaptability for various pH, OII amount, PMS concentration, catalyst dosage and inorganic anions (Cl^-, HCO_3^-, $H_2PO_4^-$, SO_4^{2-}, NO_3^-). This work provides a superior AOPs catalyst for recalcitrant wastewater remediation and an important novel AOPs system based on Co-MGs.

Acknowledgements This work was financially supported by the National Key R&D Program of China (No. 2021YFB3802800), the National Natural Science Foundation of China (Nos. 52101195 and 51871120), the Natural Science Foundation of Jiangsu Province (Nos. BK20190480 and BK20200019), the National Key R&D Program of China (No. 2021YFB3802800) and the Fundamental Research Funds for the Central Universities (Nos. 30920021156 and 30920010004).

Declarations

Conflict of interests The authors declare that they have no conflict of interest.

References

[1] Jia Z, Duan XG, Qin P, Zhang WC, Wang WM, Yang C, Sun HQ, Wang SB, Zhang LC. Disordered atomic packing structure of metallic glass: toward ultrafast hydroxyl radicals production rate and strong electron transfer ability in catalytic performance. Adv Func Mater. 2017;27(38):1702258. https://doi.org/10.1002/adfm.201702258.

[2] Ying HQ, Liu SN, Wu ZD, Dong WX, Ge JC, Hahn H, Lan S. Phase selection rule of high-entropy metallic glasses with different short-to-medium-range orders. Rare Met. 2022;41(6):2021. https://doi.org/10.1007/s12598-022-01973-8.

[3] Sheng HW, Luo KW, Alamgir FM, Bai JM, Ma E. Atomic packing and short-to-medium-range order in metallic glasses. Nature. 2006;439(7075):419. https://doi.org/10.1038/nature04421.

[4] Lan S, Zhu L, Wu ZD, Gu L, Zhang QH, Kong HH, Liu JZ, Song RY, Liu SN, Sha WYG, Liu Q, Liu W, Wang PY, Liu CT, Ren Y, Wang XL. A medium-range structure motif linking amorphous and crystalline states. Nat Mater. 2021;20(10):1347. https://doi.org/10.1038/s41563-021-01011-5.

[5] Lan S, Ren Y, Wei XY, Wang B, Gilbert EP, Shibayama T, Watanabe S, Ohnuma M, Wang XL. Hidden amorphous phase and reentrant supercooled liquid in Pd-Ni-P metallic glasses. Nat Commun. 2017;8:14679. https://doi.org/10.1038/ncomms14679.

[6] Han KM, Jiang H, Wang YM, Qiang JB. Zr-Ti-Al-Fe-Cu bulk metallic glasses for biomedical device application. Rare Met. 2021;40(5):1239. https://doi.org/10.1007/s12598-020-01644-6.

[7] Jia Z, Zhang WC, Wang WM, Habibi D, Zhang LC. Amorphous $Fe_{78}Si_9B_{13}$ alloy: an efficient and reusable photo-enhanced Fenton-like catalyst in degradation of cibacron brilliant red 3B-A dye under UV–vis light. Appl Catal B. 2016;192:46. https://doi.org/10.1016/j.apcatb.2016.03.048.

[8] Zhang SY, Gao YY, Zhang ZB, Gu T, Liang XB, Wang LZ. Research progress on functional properties of novel high-entropy metallic glasses. Chin J Rare Met. 2021;45(6):717. https://doi.org/10.13373/j.cnki.cjrm.XY20080032.

[9] Jia Z, et al. Surface aging behaviour of Fe-based amorphous alloys as catalysts during heterogeneous photo Fenton-like process for water treatment. Appl Catal B. 2017;204:537. https://doi.org/10.1016/j.apcatb.2016.12.001.

[10] Ying HQ, Liu SN, Wu ZD, Dong WX, Ge JC, Hahn H, Provenzano V, Wang XL, Lan S. Phase selection rule of high-entropy metallic glasses with different short--to-medium-range orders. Rare Met. 2022;41(6):2021. https://doi.org/10.1007/s12598-022-01973-8.

[11] Zhang LB, Qiu LX, Zhu QY, Liang X, Huang JX, Yang MT, Zhang ZX, Ma J, Shen J. Insight into efficient degradation of 3,5-dichlorosalicylic acid by Fe-Si-B amorphous ribbon under neutral condition. Appl Catal B. 2021;294:120258. https://doi.org/10.1016/j.apcatb.2021.120258.

[12] Chen S, Yang GN, Luo ST, Yin SJ, Jia JL, Li Z, Gao SH, Shao Y, Yao KF. Unexpected high performance of Fe-based nanocrystallized ribbons for azo dye decomposition. J Mater Chem A. 2017;5(27):14230. https://doi.org/10.1039/c7ta01206c.

[13] Liang SX, Zhang WC, Zhang L, Wang WM, Zhang LC. Remediation of industrial contaminated water with arsenic and nitrate by mass-produced Fe-based metallic glass: toward potential industrial applications. Sustain Mater Technol. 2019;22:e00126. https://doi.org/10.1016/j.susmat.2019.e00126.

[14] Jiang JL, Jia Z, He Q, Wang Q, Yu FL, Zhang LC, Liang SX, Kruzic JJ, Lu J. Synergistic function of iron and cobalt in metallic glasses for highly improving persulfate activation in water treatment. J Alloy Compd. 2020;822:153574. https://doi.org/10.1016/j.jallcom.2019.153574.

[15] Xu H, Jiang N, Wang D, Wang LH, Song YF, Chen ZQ, Ma J, Zhang T. Improving PMS oxidation of organic pollutants by single cobalt atom catalyst through hybrid radical and non-radical pathways. Appl Catal B. 2020;263:118350. https://doi.org/10.1016/j.apcatb.2019.118350.

[16] Lu H, Sui MH, Yuan BJ, Wang JY, Lv YN. Efficient degradation of nitrobenzene by Cu-Co-Fe-LDH catalyzed peroxymonosulfate to produce hydroxyl radicals. Chem Eng J. 2019;357:140. https://doi.org/10.1016/j.cej.2018.09.111.

[17] Ahn YY, Bae H, Kim HI, Kim SH, Kim JH, Lee SG, Lee J. Surface-loaded metal nanoparticles for peroxymonosulfate activation: efficiency and mechanism reconnaissance. Appl Catal B. 2019;241:561. https://doi.org/10.1016/j.apcatb.2018.09.056.

[18] Wei J, Han D, Bi JT, Gong JB. Fe-doped ilmenite $CoTiO_3$ for antibiotic removal: electronic modulation and enhanced activation of peroxymonosulfate. Chem Eng J. 2021;423:130165. https://doi.org/10.1016/j.cej.2021.130165.

[19] Qin XD, Zhu ZW, Liu G, Fu HM, Zhang HW, Wang AM, Li H, Zhang HF. Ultrafast degradation of azo dyes catalyzed by cobalt-based metallic glass. Sci Rep. 2015;5:18226. https://doi.org/10.1038/srep18226.

[20] Zeng D, Dan ZH, Qin FX, Chang H. Adsorption-enhanced reductive degradation of methyl orange by $Fe_{73.3}Co_{10}Si_4B_8P_4Cu_{0.7}$ amorphous alloys. Mater Chem Phys. 2020;242:122307. https://doi.org/10.1016/j.matchemphys.2019.122307.

[21] Tang Y, Shao Y, Chen N, Liu X, Chen SQ, Yao KF. Insight into the high reactivity of commercial Fe–Si–B amorphous zero-valent iron in degrading azo dye solutions. RSC Adv. 2015;5(43):34032. https://doi.org/10.1039/c5ra02870a.

[22] Chen SQ, Chen N, Chen MT, Luo ST, Shao Y, Yao KF. Multi-phase nanocrystallization induced fast degradation of methyl orange by annealing Fe-based amorphous ribbons. Intermetallics. 2017;90:30. https://doi.org/10.1016/j.intermet.2017.06.009.

[23] Wang JC, Jia Z, Liang SX, Qin P, Zhang WC, Wang WM, Sercombe TB, Zhang LC. $Fe_{73.5}Si_{13.5}B_9Cu_1Nb_3$ metallic glass: rapid activation of peroxymonosulfate towards ultrafast Eosin Y degradation. Mater Des. 2018;140:73. https://doi.org/10.1016/j.matdes.2017.11.049.

[24] Liang SX, Zhang QY, Jia Z, Zhang WC, Wang WM, Zhang LC. Tailoring surface morphology of heterostructured iron-based Fenton catalyst for highly improved catalytic activity. J Colloid Interface Sci. 2021;581:860. https://doi.org/10.1016/j.jcis.2020.07.138.

[25] Zhang LF, Zhang LH, Sun YL, Jiang B. Porous ZrO_2 encapsulated perovskite composite oxide for organic pollutants removal: enhanced catalytic efficiency and suppressed metal leaching. J Colloid Interface Sci. 2021;596:455.

[26] Tang MF, Lai LM, Ding DY, Liu TH, Kang WZ, Guo N, Song B, Guo SF. Rapid degradation of Direct Blue dye by Co-based amorphous alloy wire. J Non-Cryst Solids. 2022;576:121282. https://doi.org/10.1016/j.jnoncrysol.2021.121282.

[27] Yang J, Li P, Duan XG, Zeng DQ, Ma ZB, An SR, Dong LQ, Cen WL, He YL. Insights into the role of dual reaction sites for single Ni atom Fenton-like catalyst towards degradation of various organic contaminants. J Hazard Mater. 2022;430:128463. https://doi.org/10.1016/j.jhazmat.2022.128463.

[28] Yuan R, Ramjaun SN, Wang ZH, Liu JS. Effects of chloride ion on degradation of Acid Orange 7 by sulfate radical-based advanced oxidation process: implications for formation of chlorinated aromatic compounds. J Hazard Mater. 2011;196:173. https://doi.org/10.1016/j.jhazmat.2011.09.007.

[29] Huang Y, Sheng B, Wang ZH, Liu QZ, Yuan RX, Xiao DX, Liu JS. Deciphering the degradation/chlorination mechanisms of maleic acid in the Fe (II)/peroxymonosulfate process: an often overlooked effect of chloride. Water Res. 2018;145:453. https://doi.org/10.1016/j.watres.2018.08.055.

[30] Huang Y, Wang ZH, Liu QZ, Wang XX, Yuan ZJ, Liu JS. Effects of chloride on PMS-based pollutant degradation: a substantial discrepancy between dyes and their common decomposition intermediate (phthalic acid). Chemosphere. 2017;187:338. https://doi.org/10.1016/j.chemosphere.2017.08.120.

[31] Bennedsen LR, Muff J, Søgaard EG. Influence of chloride and carbonates on the reactivity of activated persulfate. Chemosphere. 2012;86(11):1092. https://doi.org/10.1016/j.chemosphere.2011.12.011.

[32] Zheng H, Bao JG, Huang Y, XiangFaheem LJ, Ren BG, Du JK, Nadagouda MN, Dionysiou DD. Efficient degradation of atrazine with porous sulfurized Fe_2O_3 as catalyst for peroxymonosulfate activation. Appl Catal B. 2019;259:118056. https://doi.org/10.1016/j.apcatb.2019.118056.

[33] Yang S, Wang P, Yang X, Shan L, Zhang WY, Shao XT, Niu R. Degradation efficiencies of azo dye Acid Orange 7 by the interaction of heat, UV and anions with common oxidants: persulfate, peroxymonosulfate and hydrogen peroxide. J Hazard Mater. 2010;179(1–3):552. https://doi.org/10.1016/j.jhazmat.2010.03.039.

[34] Li J, Wan YJ, Li YJ, Yao G, Lai B. Surface Fe(III)/Fe(II) cycle promoted the degradation of atrazine by peroxymonosulfate activation in the presence of hydroxylamine. Appl Catal B. 2019;256:117782. https://doi.org/10.1016/j.apcatb.2019.117782.

[35] Long X, Feng CP, Ding DH, Chen N, Yang SJ, Chen GY, Wang XM, Chen RZ. Oxygen vacancies-enriched $CoFe_2O_4$ for peroxymonosulfate activation: the reactivity between radical-non-radical coupling way and bisphenol A. J Hazard Mater. 2021;418:126357. https://doi.org/10.1016/j.jhazmat.2021.126357.

[36] Wei B, Li XL, Sun HG, Song KK, Wang L. Comparative study on the corrosion and self-cleaning behavior of Fe-B-C and Fe-B-P amorphous alloys in methylene blue dye solution degradation. J Non-Cryst Solids. 2022;575:121212. https://doi.org/10.1016/j.jnoncrysol.2021.121212.

[37] Wang Q, Chen MX, Lin PH, Cui ZQ, Chu CL, Shen BL. Investigation of FePC amorphous alloys with self-renewing behaviour for highly efficient decolorization of methylene blue. J Mater Chem A. 2018;6(23):10686. https://doi.org/10.1039/c8ta01534a.

[38] Gu JL, Shao Y, Zhao SF, Lu SY, Yang GN, Chen SQ, Yao KF. Effects of Cu addition on the glass forming ability and corrosion resistance of Ti-Zr-Be-Ni alloys. J Alloy Compd. 2017;725:573. https://doi.org/10.1016/j.jallcom.2017.07.165.

[39] Pratap A, Kasyap K, Prajapati S, Upadhyay D. Bio-corrosion studies of Fe-based metallic glasses. Mater Today: Proc. 2021;42:1669. https://doi.org/10.1016/j.matpr.2020.07.588.

[40] Zhou XC, Tang YL, Xu XF, Zhou XQ, Zhao GQ, Zhou MF, Wan GP, Wang GZ. CoP/C hollow hybrids inducing abundant active interfaces and fast electron transfers to activate peroxymonosulfates for bisphenol A degradation. Materials Today Nano. 2021;14:100116. https://doi.org/10.1016/j.mtnano.2021.100116.

[41] Fan J, Qin H, Jiang S. Mn-doped g-C_3N_4 composite to activate peroxymonosulfate for acetaminophen degradation: the role of superoxide anion and singlet oxygen. Chem Eng J. 2019;359:723. https://doi.org/10.1016/j.cej.2018.11.165.

[42] Yang Y, Banerjee B, Brudvig GW, Kim JH, Pignatello JJ. Oxidation of organic compounds in water by unactivated peroxymonosulfate. Environ Sci Technol. 2018;52(10):5911. https://doi.org/10.1021/acs.est.8b00735.

[43] Nguyen TB, Huang CP, Doong RA, Wang MH, Chen CW, Dong CD. Manipulating the morphology of 3D flower-like $CoMn_2O_4$ bimetallic catalyst for enhancing the activation of peroxymonosulfate toward the degradation of selected persistent pharmaceuticals in water. Chem Eng J. 2022;436:135244. https://doi.org/10.1016/j.cej.2022.135244.

[44] Qi Y, Li J, Zhang YQ, Cao Y, Si YM, Wu ZR, Muhammad Akram, Xing Xu. Novel lignin-based single atom catalysts as peroxymonosulfate activator for pollutants degradation: role of single cobalt and electron transfer pathway. Appl Catal B. 2021;286:119910. https://doi.org/10.1016/j.apcatb.2021.119910.

[45] Zhu MP, Yang JCE, Sun DD, Yuan BL, Fu ML. Deciphering the simultaneous removal of carbamazepine and metronidazole by monolithic Co_2AlO_4@Al_2O_3 activated peroxymonosulfate. Chem Eng J. 2022;436:135201. https://doi.org/10.1016/j.cej.2022.135201.

[46] Fu S, Liu SN, Ge JC, Wang JJ, Ying HQ, Wu SS, Yan MY, Zhu L, Ke YB, Luan JH, Ren Y, Zuo XB, Wu ZD, Peng Z, Liu CT, Wang XL, Feng T, Lan S. In situ study on medium-range order evolution during the polyamorphous phase transition in a Pd-Ni-P nanostructured glass. J Mater Sci Technol. 2022;125:12. https://doi.org/10.1016/j.jmst.2022.01.038.

[47] Wang JC, Liang SX, Jia Z, Zhang WC, Wang WM, Liu YJ, Lu J, Zhang LC. Chemically dealloyed Fe-based metallic glass with void channels-like architecture for highly enhanced peroxymonosulfate activation in catalysis. J Alloy Compd. 2019;785:642. https://doi.org/10.1016/j.jallcom.2019.01.130.

[48] Jia Z, Jia Z, Wang Q, Sun LG, Wang Q, Zhang LC, Wu G, Luan JH, Jiao ZB, Wang A, Liang SX, Gu M, Lu J. Attractive in situ self-reconstructed hierarchical gradient structure of metallic glass for high efficiency and remarkable stability in catalytic performance. Adv Func Mater. 2019;29(19):1807857. https://doi.org/10.1002/adfm.201807857.